electronics

MDPI

Article

Adaptive Pilot-Assisted Channel Estimation for OFDM-Based High-Speed Railway Communications

Khoi Van Nguyen, Toan Thanh Dao and Do Viet Ha *

Faculty of Electrical-Electronic Engineering, University of Transport and Communications (UTC), Hanoi 10000, Vietnam; nvkhoi@utc.edu.vn (K.V.N.); daotoan@utc.edu.vn (T.T.D.)
* Correspondence: dovietha@utc.edu.vn

Abstract

This paper investigates an adaptive pilot-assisted channel estimation framework for orthogonal frequency-division multiplexing (OFDM)-based high-speed railway (HSR) communications over non-stationary wideband channels. Within this framework, a channel-aware adaptive pilot insertion (CA-API) mechanism is combined with an linear minimum mean square error (LMMSE) shrinkage technique to adjust pilot density based on temporal channel variations. Using the refined pilot-domain observations, three time-domain channel estimators namely piecewise cubic Hermite interpolation (PCHIP), autoregressive (AR), and Gaussian process regression (GPR), are comparatively evaluated under measurement-based HSR channel models. Simulation results across Remote Area (RA), Closer Area (CEA), and Close Area (CA) conditions demonstrate that the benefit of adaptive pilot scheduling is strongly scenario-dependent. In RA and CEA, the CA-API scheme reduces overhead while maintaining channel reconstruction accuracy close to that of the fixed-pilot baseline, with average overhead reductions of 38% and 30%, respectively. Under the more dispersive CA condition, the adaptive mechanism tends to increase pilot density to preserve reliable channel tracking. Among the evaluated algorithms, GPR delivers the highest estimation accuracy, AR provides a balanced trade-off between accuracy and implementation complexity, and PCHIP is less accurate but remains attractive because of its low complexity. This study provides practical insights into the joint design of adaptive pilot scheduling and channel estimation for HSR wireless communication systems.

Keywords: high-speed railway; non-stationary channel; channel estimation; pilot adaptation

1. Introduction

High-speed railway (HSR) communications are required to support both reliable railway operation and high-capacity passenger services under extreme mobility [1]. In OFDM-based HSR systems, channel state information (CSI) estimation is particularly challenging due to severe Doppler spread, rapid time variation, and frequency-selective fading [2,3]. Moreover, recent investigations have shown that rapidly changing channels in HSR scenarios demand considerable pilot overhead, with Inter-Carrier Interference (ICI) significantly undermining the performance of traditional linear and interpolation-based estimators [4].

Despite extensive research on high-mobility channel estimation, many studies still rely on simplified assumptions, such as Rician fading in [5,6], Rayleigh fading in [7], and simplified cascaded time-varying channel modeling in [8]. Even in HSR-specific studies, benchmark or simulation-oriented channel models are still commonly used. The WINNER II D2a scenario is adopted in [1,2,9], whereas studies [10,11] employ 3GPP-based channel settings.

Check for updates

Academic Editor: Hector E. Nistazakis

Received: 12 March 2026
Revised: 1 May 2026
Accepted: 4 May 2026
Published: 8 May 2026

Copyright: © 2026 by the authors. Licensee MDPI, Basel, Switzerland. This article is an open access article distributed under the terms and conditions of the Creative Commons Attribution (CC BY) license.

More recently, the extended vehicular A channel model and a quasi-stationary channel spreading function (CSF) assumption have also been used for CSF-inspired channel transfer function estimation in high-mobility OFDM systems [12]. While these models are useful for standardized evaluation, they may not fully capture the strong LoS component [13], non-stationary behavior [14], and scenario-dependent Doppler characteristics [10,14] observed in practical HSR propagation. This motivates the use of a non-stationary wideband HSR channel model parameterized using measurement data, so that the resulting performance evaluation can better reflect practical HSR propagation conditions.

Another important challenge lies in pilot design. In rapidly time-varying channels, dense pilot insertion is often required to maintain channel tracking quality [4,9], but this directly increases pilot overhead and reduces spectral efficiency [15–17]. Therefore, channel estimation in HSR-OFDM systems should be studied not only from the perspective of estimation accuracy but also from the trade-off between channel reconstruction performance and pilot resource consumption.

In the category of conventional approaches, estimators such as Least Squares (LS), Linear Minimum Mean Square Error (LMMSE), Enhanced LMMSE (E-LMMSE), DFT-based LS/LMMSE, and various interpolation methods remain widely adopted because of their clear structure and ease of implementation [5,18], while E-LMMSE has been further developed as an enhanced variant of LMMSE [11]. Specifically, the work in [11] exploits multi-path Doppler Frequency Offset (DFO) estimation to refine the correlation matrix of the LMMSE filter in a two-tap High-Speed Railway (HSR) channel with severe Doppler effects. However, the method still exhibits an error floor at high Signal-to-Noise Ratio (SNR) levels because Inter-Carrier Interference (ICI) is not fully eliminated. Similarly, studies comparing LS, LMMSE, and SVD-MMSE with spline interpolation in high-speed channels show that, although LMMSE provides good estimation accuracy, its computational complexity remains high, while LS degrades significantly as the Doppler shift increases in the absence of an effective ICI mitigation mechanism [5]. These conventional estimators are typically assessed under simplified benchmark channels, which facilitate algorithm comparison but do not fully capture the non-stationary and scenario-dependent nature of practical HSR propagation.

Alternatively, recent research has shifted toward deep learning models such as cGAN [1], 1D-CNN [2], Bi-GRU, GCE-RNN [19], CNN-BiLSTM-Attention [10], MAML [6], SRDnN [20], or hybrid architectures like Attention-Aided MMSE [21] to enhance channel estimation performance in high-mobility environments. These methods often outperform LS/MMSE under conditions of high Doppler shifts, limited pilot overhead, or complex non-linear channel structures. For instance, N2N-cGAN and 1D-CNN approaches for HSR utilize the WINNER II D2a benchmark and demonstrate significant accuracy improvements over traditional LS [1,2]. However, recent AI surveys have also identified several common drawbacks of this class of methods, including strong dependence on training data, the risk of overfitting, limited interpretability [22,23], high resource consumption, difficulty in edge deployment [10], and degraded generalization when the SNR or propagation environment deviates from the training domain [10,22]. Furthermore, some models require strict pilot synchronization [10] or periodic retraining when the environment changes [2].

From the perspective of pilot design, several studies have proposed adaptive pilot patterns for doubly selective non-stationary channels [17] or combined sparse pilot structures with deep learning/LSTM-based estimators [24,25]. However, these works typically assume ideal synchronization or focus on pilot reduction with the support of complex AI-based models. As a result, there is still a lack of studies that investigate an adaptive pilot mechanism together with time-domain estimators that are structurally trans-

parent, do not require large-scale offline training, and still provide sufficient diversity in processing principles.

These limitations motivate the investigation of lower-complexity alternatives that can operate effectively under sparse pilot observations without relying on extensive offline training. Within this scope, three representative time-domain channel estimation (TDCE) methods are selected for comparison: piecewise cubic Hermite interpolation (PCHIP), symbol-domain autoregressive tracking (AR), and Gaussian process regression (GPR). These methods represent three distinct reconstruction paradigms, including deterministic interpolation, statistical signal tracking, and probabilistic machine learning, respectively. As highlighted by recent survey-based evidence, complex neural-network-based estimators often suffer from a strict reliance on large datasets and a lack of interpretability [23]. To overcome these issues, Gaussian Process Regression (GPR) emerges as an effective alternative that is especially suitable for sparse pilot observations, as it works efficiently with small datasets and retains a transparent model-based structure while still providing competitive performance [26].

This paper develops a practical evaluation framework for HSR-OFDM channel estimation that combines realistic channel modeling, pilot-resource adaptation under high mobility, and comparative estimator evaluation. In contrast to data-driven neural estimators that require offline training and architecture-specific tuning, this work focuses on transparent, training-free estimators for pilot-assisted channel reconstruction. Specifically, a measurement-based non-stationary wideband HSR channel model is adopted [27,28], the proposed channel-aware adaptive pilot insertion (CA-API) mechanism is introduced to adjust pilot density according to channel variation, and an LMMSE shrinkage refinement is further applied to enhance the reliability of pilot-domain channel estimates. Based on this refined pilot-domain information, three TDCE methods are comparatively evaluated for HSR-OFDM systems: PCHIP, AR, and GPR. The framework is then assessed under the RA, CEA, and CA conditions, which correspond to different propagation environments and multipath characteristics, ranging from sparse LoS-dominant propagation to more severe delay dispersion and richer multipath effects [29].

The main contributions of this paper are summarized as follows:

1. An HSR-OFDM evaluation framework is established based on a measurement-based non-stationary channel model, instead of simplified Rayleigh/Rician assumptions or standardized benchmark models.
2. A pilot-domain enhancement strategy is developed by combining the proposed channel-aware adaptive pilot insertion (CA-API) mechanism with LMMSE shrinkage refinement in order to reduce pilot overhead while improving the reliability of channel observations under high-mobility conditions.
3. Three TDCE methods, PCHIP, AR, and GPR, are comparatively evaluated under the same adaptive pilot framework to clarify their trade-offs in estimation accuracy and implementation complexity.
4. The proposed framework is evaluated under three representative HSR scenarios to clarify how different propagation conditions affect the trade-off between estimation accuracy and pilot overhead.

The results show that the benefit of adaptive pilot scheduling is highly scenario-dependent. The most favorable trade-off is obtained in the RA scenario, where the NMSE remains close to that of the fixed-pilot scheme while the pilot overhead is significantly reduced. In the CEA scenario, adaptive pilot insertion is still beneficial, but the overhead-saving gain gradually decreases as the SNR increases. By contrast, in the CA scenario, the adaptive scheme becomes less attractive because the pilot overhead approaches, or even exceeds, that of the fixed scheme, while the NMSE improvement remains limited.

In terms of channel estimation, GPR delivers the best NMSE in all scenarios, AR achieves moderate performance, and PCHIP is the most robust when pilot density is reduced. These results indicate that pilot scheduling and channel estimation should be jointly designed to achieve a favorable trade-off between estimation accuracy and pilot overhead in HSR-OFDM systems.

The remainder of this paper is organized as follows. Section 2 presents the non-stationary wideband HSR channel model and the OFDM system configuration. Section 3 describes the adaptive pilot-assisted mechanism and the three evaluated TDCE methods. Section 4 analyzes the numerical results under the RA, CEA, and CA scenarios. Finally, Section 5 concludes the paper.

2. System Model

2.1. Non-Stationary Wideband HSR Channel Model

To enhance transmission quality in HSR communication systems, moving relay stations (MRSs) mounted on trains are used to improve connectivity. The architecture comprises two links as depicted in Figure 1: (1) the outdoor link between the base station (BS) and the MRS and (2) the indoor link between the MRS and the on-board mobile station (MS). This study focuses on modeling and evaluating the outdoor propagation channel.

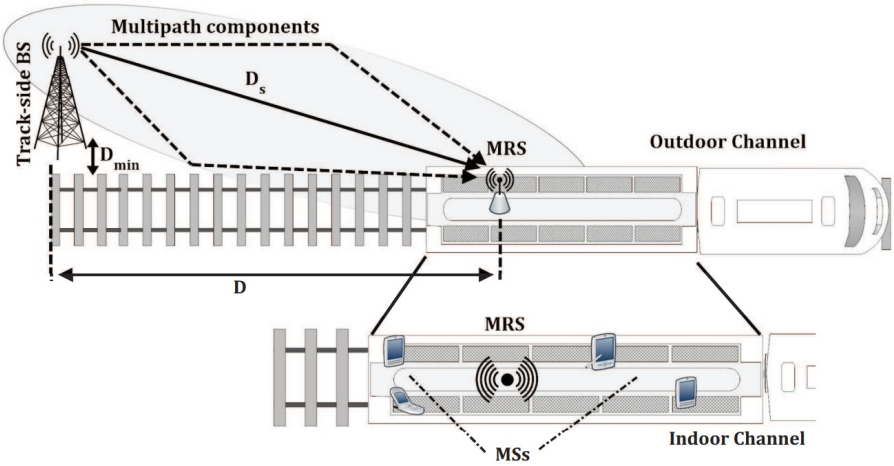


Figure 1. HSR communication system implementing MRS.

The HSR channel is modeled using a geometry-based stochastic model (GBSM) with a confocal ellipse structure, where the BS and the train are assumed to be located at the two foci as shown in Figure 2. The total number of delay paths (taps) corresponds to the number of ellipses I in the model. The time-varying distance between the BS and the MRS, denoted by $D_s(t)$, is given by

$$D_s(t) = \sqrt{D_{\min}^2 + D^2(t)}. \tag{1}$$

Here, $D_{\min}$ represents the minimum distance from the BS to the railway track, and $D(t)$ is the projection of this distance onto the track axis. For each delay path i, the scatterers N_i are assumed to be distributed on the corresponding ellipse. In the ellipse-based GBSM, N_i denotes the number of effective scatterers used to realize the i-th delay path in the simulator. In this study, we set $N_i = 32$ for all delay paths and keep this value fixed across RA, CEA, and CA in order to ensure a consistent comparison among scenarios while maintaining moderate simulation complexity. This choice is also consistent with the reference non-stationary HSR channel model [27], where a finite setting with $N_i = 32$ is used in the autocorrelation function (ACF) comparison under HSR operation at 350 km/h. The differ-

ence in multipath richness among the considered scenarios is therefore mainly captured by the measurement-based PDP characteristics, including the number of significant taps, tap powers, and delay spread, rather than by varying N_i itself.

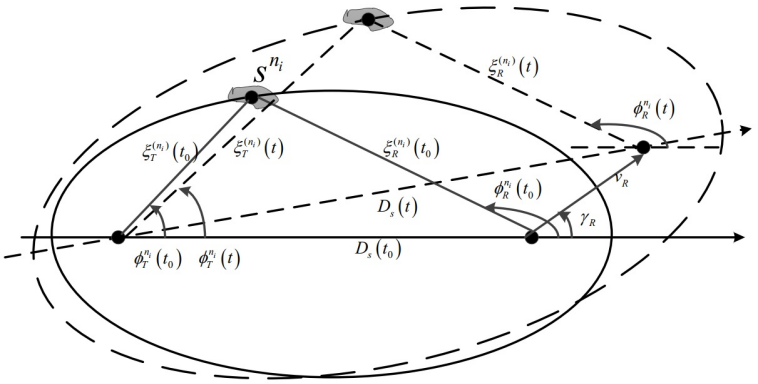


Figure 2. The geometrical ellipse model for HSR channels.

The geometric parameters of the ellipse, including the semi-major axis $a_i(t)$ and the semi-minor axis $b_i(t)$, are determined based on the distance between the two foci

$$b_i(t) = \sqrt{a_i^2(t) - f_s^2(t)}, \tag{2}$$

where $f_s(t) = D_s(t)/2$ represents half the distance between the two foci.

Due to high mobility, the channel is described by a time-varying impulse response $h(t, \tau)$ as

$$h(t, \tau) = \sum_{i=1}^{I} h_i(t)\delta(\tau - \tau_i). \tag{3}$$

In this expression, $h_i(t)$ and τ_i are the complex gain and propagation delay of the ith path, respectively. The complex gain $h_i(t)$ is formed by two main signal components: (i) the Line-of-Sight (LoS) component, characterized by the Rician (K) factor and the maximum Doppler frequency $f_{\max}$, and (ii) the single-bounced (SB) scattering component, which captures the impact of scatterers on the average received signal energy, denoted by Ω_i.

The LoS component models the direct BS–MRS path and is present only in the first delay tap $(i = 1)$:

$$h_1^{\mathrm{LoS}}(t) = \sqrt{\frac{K}{K+1}} \exp\Big(j\Big(2\pi f_{\max} t \cos\left(\phi^{\mathrm{LoS}}(t)\right) + \psi_0\Big)\Big), \tag{4}$$

where $\phi^{\mathrm{LoS}}(t)$ is the time-varying angle of arrival (AoA) and $\psi_0 \sim \mathcal{U}[0, 2\pi)$ is the initial phase.

The SB component models multipath contributions from N_i scatterers on the i-th ellipse. The scattered gain of the i-th tap is

$$h_i^{\mathrm{SB}}(t) = \sqrt{\frac{1}{(K+1)N_i}} \sum_{n=1}^{N_i} \exp\Big(j\Big(2\pi f_{\max} t \cos\left(\phi_{n,i}(t)\right) + \psi_{n,i}\Big)\Big), \tag{5}$$

where N_i is the number of effective scatterers, $\phi_{n,i}(t)$ is the time-varying AoA of the n-th scattered path, and $\psi_{n,i} \sim \mathcal{U}[0, 2\pi)$ is the i.i.d. random phase. For $i > 1$, K is typically set to 0, yielding $h_i(t) = h_i^{\mathrm{SB}}(t)$.

The angle of arrival (AoA) varies continuously over time due to train motion. The AoA of the LoS component, $\phi^{\mathrm{LoS}}(t)$, is computed from the relative position and the train speed. For the scattering components, the AoA $\phi_R^{(n_i)}(t)$ is modeled using the von Mises probability

density function, which enables controlling the angular spread via the concentration parameter $\kappa_R^{(i)}$. To accurately determine these angles, the modified equal-area method (MMEA) is applied and combined with real measurement-based power delay profile (PDP) data, ensuring the model's realism.

This work adopts a measurement-based non-stationary wideband HSR channel model in order to better capture practical HSR propagation conditions than simplified Rayleigh/Rician assumptions or purely standardized benchmark profiles. In particular, the measured power delay profiles (PDPs) for the RA, CEA, and CA scenarios are used to parameterize the geometry-based stochastic model, thereby enabling different channel conditions to be represented consistently in terms of tap structure, delay spread, and multipath richness. Under this framework, the RA scenario corresponds to relatively sparse and LoS-dominant propagation, whereas CEA and especially CA exhibit richer multipath and stronger delay dispersion. These measured PDP data are further combined with the confocal-ellipse channel structure and time-varying angular statistics to generate non-stationary wideband HSR channel realizations for performance evaluation.

2.2. OFDM Signal Model

Consider an OFDM system with N_c subcarriers and system bandwidth B. The sampling interval is defined as $T_s = 1/B$. The transmitted frequency-domain symbol vector at the i-th OFDM symbol is given by

$$\mathbf{X}^{(i)} = \left[X_0^{(i)}, X_1^{(i)}, \ldots, X_{N_c-1}^{(i)}\right]^T, \tag{6}$$

where $X_k^{(i)}$ is the data symbol on the k-th subcarrier. After the inverse fast Fourier transform (IFFT), the corresponding time-domain OFDM signal is expressed as

$$x_n^{(i)} = \frac{1}{N_{\mathrm{FFT}}} \sum_{k=0}^{N_{\mathrm{FFT}}-1} X_k^{(i)} e^{j2\pi kn/N_{\mathrm{FFT}}}, \qquad n = 0, 1, \ldots, N_{\mathrm{FFT}} - 1. \tag{7}$$

After guard interval insertion, the transmitted OFDM block passes through a time-varying multipath channel. Let $h^{(i)}(l, n)$ denote the channel coefficient of the l-th path at time index n within the i-th OFDM symbol, where $l = 0, 1, \ldots, L-1$, and let $w^{(i)}(n)$ denote the additive white Gaussian noise. The received time-domain signal can then be written as

$$y^{(i)}(n) = \sum_{l=0}^{L-1} h^{(i)}(l, n)\, x^{(i)}(n - l) + w^{(i)}(n). \tag{8}$$

After removing the guard interval and applying the FFT, the received signal on the k-th subcarrier is obtained as

$$Y_k^{(i)} = \sum_{m=0}^{N_{\mathrm{FFT}}-1} H_{k,m}^{(i)} X_m^{(i)} + W_k^{(i)}, \qquad k = 0, 1, \ldots, N_{\mathrm{FFT}} - 1, \tag{9}$$

where $W_k^{(i)}$ is the frequency-domain noise component, and $H_{k,m}^{(i)}$ is the effective channel coefficient from subcarrier m to subcarrier k. In matrix form,

$$\mathbf{Y}^{(i)} = \mathbf{H}^{(i)} \mathbf{X}^{(i)} + \mathbf{W}^{(i)}, \tag{10}$$

where $\mathbf{H}^{(i)} \in \mathbb{C}^{N_{\mathrm{FFT}} \times N_{\mathrm{FFT}}}$ is the effective frequency-domain channel matrix. If the channel were constant within one OFDM symbol, $\mathbf{H}^{(i)}$ would become nearly diagonal. In HSR environments, however, the channel may vary significantly within one symbol duration,

so the off-diagonal elements of $\mathbf{H}^{(i)}$ become non-negligible and introduce inter-carrier interference (ICI) [3]. Therefore, accurate channel estimation in the time domain is essential not only for recovering the channel response itself but also for mitigating the ICI caused by fast channel variation.

3. Time-Domain Channel Estimation for HSR Systems

3.1. Proposed Channel-Aware Adaptive Pilot Insertion

To estimate the channel in rapidly time-varying HSR environments, this paper employs a time-domain pilot structure. In this structure, each pilot symbol P is inserted between two zero guard intervals (ZGIs) of length N_G. The preceding ZGI suppresses inter-symbol interference (ISI), whereas the following ZGI provides an observation region for collecting the multipath components of the channel impulse response (CIR) without overlapping with the subsequent data symbol [3].

For pilot-assisted estimation, let $\mathcal{P}$ denote the set of pilot positions. At a pilot position $(k, i) \in \mathcal{P}$, the received symbol can be written as

$$Y_k^{(i)} = H_k^{(i)} P_k^{(i)} + \eta_k^{(i)}, \tag{11}$$

where $P_k^{(i)}$ is the known pilot symbol, $H_k^{(i)}$ is the corresponding channel response, and $\eta_k^{(i)}$ includes noise and residual interference. A pilot-domain least-squares (LS) estimate is therefore obtained as

$$\hat{H}_k^{\mathrm{LS},(i)} = \frac{Y_k^{(i)}}{P_k^{(i)}}, \qquad (k, i) \in \mathcal{P}. \tag{12}$$

To improve robustness under low-SNR conditions, the LS estimate is further refined using LMMSE shrinkage. In its general form, the LMMSE estimate is given by [26]

$$\hat{\mathbf{h}}_{\mathrm{LMMSE}} = \mathbf{R}_{hh}\left(\mathbf{R}_{hh} + \sigma_n^2 (\mathbf{X}^H \mathbf{X})^{-1}\right)^{-1} \hat{\mathbf{h}}_{LS}, \tag{13}$$

where the weighting matrix is determined by the channel correlation and noise statistics. Under the assumption that channel taps are independently processed, the above matrix form can be reduced to a tap-wise shrinkage expression

$$\hat{h}_{\mathrm{shrink}} = \alpha_l \hat{h}_{LS}, \qquad \alpha_l = \frac{\rho_l}{\rho_l + \sigma_n^2 / P_{pilot}^2}, \tag{14}$$

where α_l is the shrinkage factor of the l-th tap, ρ_l is the average power of that tap, σ_n^2 is the noise variance, and P_{pilot} is the known pilot amplitude.

Built upon the fixed-pilot baseline, this paper proposes a Channel-Aware Adaptive Pilot Insertion (CA-API) mechanism to adjust the pilot interval according to the instantaneous channel variation. The objective is to reduce unnecessary pilot density under stable channel conditions while maintaining estimation accuracy when the channel changes rapidly.

The channel variation between two consecutive pilot instants is quantified by the normalized innovation metric

$$\epsilon = \frac{\left\| \hat{\mathbf{h}}_{now} - \hat{\mathbf{h}}_{last} \right\|^2}{\left\| \hat{\mathbf{h}}_{now} \right\|^2 + \eta}, \tag{15}$$

where $\hat{\mathbf{h}}_{now}$ and $\hat{\mathbf{h}}_{last}$ denote the CIR vectors at the current pilot instant and the nearest previous pilot instant, respectively, and η is a small constant introduced to avoid division by zero.

Based on the value of $\epsilon(i)$, the pilot interval is adaptively updated through two thresholds, θ_L and θ_H. Specifically, when $\epsilon(i) > \theta_H$, the channel is regarded as rapidly varying and a denser pilot configuration is selected to maintain channel tracking accuracy; when $\theta_L < \epsilon(i) \leq \theta_H$, an intermediate pilot interval is adopted to balance estimation accuracy and pilot overhead; otherwise, when $\epsilon(i) \leq \theta_L$, the channel variation is considered mild and the pilot spacing is increased to improve bandwidth efficiency.

In practice, the adaptive pilot spacing is realized through a three-level set, $D_p \in \{1, 2, 3\}$, corresponding to dense, intermediate, and sparse insertion modes. Initialized at the intermediate level, this scheme provides a low-complexity yet flexible update mechanism tailored for rapidly varying HSR channels. For each pilot-bearing symbol, the pilot-domain LS estimate is refined using tap-wise LMMSE shrinkage, followed by an evaluation of the innovation metric between consecutive refined CIR vectors. The adaptation thresholds, $\theta_L = c_L\sigma_n^2$ and $\theta_H = c_H\sigma_n^2$, are configured with $c_L = 2.0$ and $c_H = 6.0$ to ensure the decision logic remains invariant to noise fluctuations. To maintain a consistent baseline for comparison across various channel scenarios (RA, CEA, and CA), these parameters are kept fixed, with a regularization constant $\eta = 10^{-12}$ integrated for numerical stability when the CIR norm becomes very small. Since η is chosen to be negligibly small relative to the signal-energy term in the denominator of Equation (15), it does not materially affect the sensitivity of pilot adaptation under the considered simulation conditions. Consequently, large, moderate, and small innovation levels trigger $D_p = 1$, $D_p = 2$, and $D_p = 3$, respectively. This hierarchy ensures that pilot-spacing decisions are governed by the innovation of refined CIR estimates, thereby mitigating the impact of noise present in raw LS observations.

3.2. Time-Domain Channel Estimation Framework

Based on the refined pilot-domain observations, the channel evolution over the OFDM frame is reconstructed using three TDCE methods: piecewise cubic Hermite interpolation (PCHIP), symbol-domain autoregressive tracking (AR), and Gaussian process regression (GPR).

3.2.1. PCHIP-Based Reconstruction

The first estimator applies piecewise cubic Hermite interpolation to the pilot-domain samples. The reconstructed channel for the l-th tap at an arbitrary time instant t is written as [30]

$$\hat{h}_l(t) = \mathcal{I}_{\text{pchip}}\Big(\{(t_i, \tilde{h}_l(t_i))\}_{i=1}^{N_p}, t\Big), \tag{16}$$

where $\mathcal{I}_{\text{pchip}}(\cdot)$ denotes the piecewise cubic Hermite interpolation operator.

PCHIP is adopted as a low-complexity interpolation baseline. Compared with cubic spline interpolation, it preserves the local trend of the pilot-domain samples and alleviates overshoot when the pilot spacing becomes nonuniform [3]. This property is particularly useful in the proposed adaptive pilot setting, where the distance between consecutive pilot-bearing symbols is not fixed.

3.2.2. Symbol-Domain Autoregressive Tracking

The second approach models the temporal evolution of each channel tap across OFDM symbols as a first-order autoregressive process. Specifically, the channel state of the l-th tap at symbol index n is expressed as

$$h_l[n] = \rho_{\text{ar}}\, h_l[n-1] + w_l[n], \qquad n = 2, \ldots, N_{\text{sym}}, \tag{17}$$

where ρ_{ar} denotes the temporal correlation coefficient and $w_l[n] \sim \mathcal{CN}(0, Q)$ is the process noise. The correlation coefficient can be related to the Doppler dynamics through [31]

$$\rho_{\text{ar}} = J_0(2\pi f_{D,\max} T_{\text{sym}}), \tag{18}$$

where $J_0(\cdot)$ is the zeroth-order Bessel function of the first kind, $f_{D,\max}$ is the maximum Doppler frequency, and T_{sym} is the OFDM symbol duration.

At symbols where pilot observations are available, the measurement model is written as

$$z_l[n] = h_l[n] + v_l[n], \tag{19}$$

with $v_l[n] \sim \mathcal{CN}(0, \sigma_n^2)$. Channel tracking is then performed by a prediction–update recursion. The prediction step is given by [31]

$$\hat{h}_l^-[n] = \rho_{\text{ar}} \hat{h}_l[n-1], \tag{20}$$

$$P^-[n] = \rho_{\text{ar}}^2 P[n-1] + Q, \tag{21}$$

where $P[n]$ denotes the estimation error variance.

Whenever a pilot observation is available, the state is refined according to

$$K[n] = \frac{P^-[n]}{P^-[n] + \sigma_n^2}, \tag{22}$$

$$\hat{h}_l[n] = \hat{h}_l^-[n] + K[n]\big(z_l[n] - \hat{h}_l^-[n]\big), \tag{23}$$

$$P[n] = \big(1 - K[n]\big) P^-[n]. \tag{24}$$

In the absence of a pilot symbol, the estimator simply propagates the predicted state forward without a measurement update.

Compared with direct interpolation between pilot-bearing symbols, the AR estimator explicitly incorporates Doppler-dependent temporal correlation into the reconstruction process. In this way, AR exploits the temporal dynamics of the HSR channel more explicitly than pure interpolation.

3.2.3. GPR-Based Reconstruction

The third approach models the temporal evolution of each channel tap as a Gaussian process and reconstructs the unknown channel values through Bayesian regression. Since $h_l(t)$ is complex-valued, the real and imaginary parts are modeled independently as

$$\Re\{h_l(t)\} \sim \mathcal{GP}\big(m_r(t), k(t,t')\big), \qquad \Im\{h_l(t)\} \sim \mathcal{GP}\big(m_i(t), k(t,t')\big). \tag{25}$$

Let

$$\mathbf{t} = [t_1, \ldots, t_{N_p}]^T, \qquad \tilde{\mathbf{h}}_{l,r} = \Big[\Re\{\tilde{h}_l(t_1)\}, \ldots, \Re\{\tilde{h}_l(t_{N_p})\}\Big]^T. \tag{26}$$

Then, the posterior mean estimate for the real part at time t is

$$\hat{h}_{l,r}(t) = m_r(t) + \mathbf{k}(t,\mathbf{t})^T \Big(\mathbf{K}(\mathbf{t},\mathbf{t}) + \sigma_n^2 \mathbf{I}\Big)^{-1} \big(\tilde{\mathbf{h}}_{l,r} - \mathbf{m}_r(\mathbf{t})\big), \tag{27}$$

and similarly for the imaginary part,

$$\hat{h}_{l,i}(t) = m_i(t) + \mathbf{k}(t,\mathbf{t})^T \Big(\mathbf{K}(\mathbf{t},\mathbf{t}) + \sigma_n^2 \mathbf{I}\Big)^{-1} \big(\tilde{\mathbf{h}}_{l,i} - \mathbf{m}_i(\mathbf{t})\big). \tag{28}$$

Therefore, the final complex-valued estimate is

$$\hat{h}_l(t) = \hat{h}_{l,r}(t) + j\hat{h}_{l,i}(t). \tag{29}$$

To reflect the Doppler-induced temporal correlation of fast-varying mobile channels, a Bessel-type kernel is adopted as

$$k(t,t') = \theta_1 J_0\big(2\pi\theta_2|t-t'|\big), \tag{30}$$

where $J_0(\cdot)$ is the zeroth-order Bessel function of the first kind, θ_1 controls the channel power scale, and θ_2 is related to the effective Doppler rate. This kernel is motivated by the Jakes autocorrelation model and has been shown to be suitable for time-varying channel estimation with pilot-symbol-assisted modulation [26]. Moreover, GPR provides the posterior variance

$$\sigma^2_{l,\mathrm{GPR}}(t) = k(t,t) - \mathbf{k}(t,\mathbf{t})^T\Big(\mathbf{K}(\mathbf{t},\mathbf{t}) + \sigma_n^2\mathbf{I}\Big)^{-1}\mathbf{k}(t,\mathbf{t}), \tag{31}$$

which quantifies the uncertainty of the reconstructed tap.

Compared with direct interpolation, GPR explicitly exploits the temporal correlation of the fading process and incorporates the noise variance into the estimation model, making it suitable for sparse pilot observations in rapidly time-varying HSR channels.

In practical implementation, the real and imaginary parts of each channel tap are reconstructed independently according to the Gaussian-process formulation in (25)–(29). For each tap, the pilot-domain observations are used as the regression inputs, and the posterior mean estimates in Equations (27) and (28) are employed for channel reconstruction, whereas the posterior variance in Equation (31) provides an additional measure of estimation uncertainty. The observation noise is incorporated through the term $(K(t,t)+\sigma_n^2 I)^{-1}$, which regularizes the regression under noisy pilot conditions. Notably, the kernel hyperparameters in Equation (30) are selected from the pilot-domain observations so that the resulting kernel remains matched to the channel power scale and the Doppler-dependent temporal correlation of the considered HSR channel realization. Under this setting, the GPR stage remains structurally transparent and directly tied to the pilot-domain observations and the assumed temporal-correlation model.

4. Simulation Results and Discussion

Table 1 summarizes the main OFDM system parameters used in the simulations. To configure the HSR channel model, we adopt measurement-based PDP settings for the considered scenarios (RA/CEA/CA). In particular, the CA scenario represents the most dispersive condition, featuring the largest number of significant taps and the maximum delay spread $\tau_{\max} = 5.6$ µs. For the CA scenario, the train-projected distance is set to $D(t) \in (250, 1550]$ m with the initial value $D(t_0) = 800$ m, and the Rician factor is set to $K = 5.9$. The PDP is further used to determine the spacing between different confocal ellipses in the geometry-based stochastic model. Moreover, the initial AoA is set to $\mu_R^{(i)}(t_0) = 45^\circ$, and the angular spread is controlled by the von Mises concentration parameter $\kappa_R^{(i)} = 6$, while the movement angle is set to $\gamma_R = 30^\circ$. The train speed is set to $v_R = 350$ km/h to represent a stringent high-mobility HSR condition with strong Doppler variation. This setting is also consistent with the adopted non-stationary HSR channel model [27], whose reference ACF comparison is reported at 350 km/h with $N_i = 32$. These parameters are used to generate the time-varying wideband HSR channel realizations for performance evaluation.

To ensure a fair comparison among the three estimators, performance is evaluated using the normalized mean square error (NMSE) of channel reconstruction. The NMSE is then defined as

$$\mathrm{NMSE} = \frac{\sum_{m=1}^{N_{\mathrm{sym}}} \sum_{l=1}^{N_P} \left| \bar{h}_l[m] - \hat{\bar{h}}_l[m] \right|^2}{\sum_{m=1}^{N_{\mathrm{sym}}} \sum_{l=1}^{N_P} \left| \bar{h}_l[m] \right|^2}, \tag{32}$$

where $\bar{h}_l[m]$ and $\hat{\bar{h}}_l[m]$ are the true and estimated channel responses for the l-th tap and the m-th symbol.

Table 1. Main OFDM simulation parameters.

Parameter	Value
System bandwidth B	10 MHz
Number of FFT points N_c	1024
Modulation order M	16 for 16-QAM
Train speed v_R	350 km/h
Fixed guard interval G_f	$\lceil B \max(\tau) \rceil$
Adaptive guard interval G_a	$\lceil B(\max(\tau) + \mathrm{std}(\tau))/2 \rceil$

To comprehensively evaluate the system performance, we employ both NMSE and SER (Symbol Error Rate) metrics to assess the end-to-end communication performance of the considered estimators. While NMSE quantifies the reconstruction accuracy of the estimated channel response, the SER reflects the practical impact of channel estimation on symbol detection. As a point of comparison, the DFT-LMMSE estimator is utilized as a robust baseline. This benchmark is selected because it effectively combines transform-domain denoising with LMMSE-based weighting, making it a well-established reference in OFDM channel estimation.

4.1. Discussion on Adaptive Pilot Results

The results in Figures 3–5 indicate that the proposed CA-API scheme maintains NMSE performance close to that of the fixed-pilot baseline in all three scenarios, confirming its reliability in tracking channel state information (CSI). In terms of resource efficiency, the pilot overhead is adjusted according to the channel condition. In the RA scenario, the adaptive scheme achieves the most significant efficiency, keeping overhead between 1.4% and 2.4%, well below the 3% fixed baseline. This represents an overhead reduction of approximately 38%. In the CEA scenario, the benefit remains visible in the low-to-medium SNR regions but gradually diminishes as SNR increases. The average overhead reduction is approximately 30%. In the CA scenario, the CA-API scheme is forced to increase pilot density (up to 5.8% at 30 dB) to combat severe fast fading and strong ICI. Consequently, the pilot overhead of the adaptive scheme exceeds that of the fixed baseline (4.5%) in the high-SNR regime, indicating that the system prioritizes estimation stability over resource saving in extreme mobility conditions. Overall, by employing an innovation metric refined by LMMSE shrinkage, the proposed method can achieve a peak pilot-overhead reduction of up to 50% in the low-SNR region while preserving reliable estimation performance, particularly in RA and CEA environments.

This trend is more clearly illustrated in Figure 6, which compares the average pilot overhead across the three scenarios. Specifically, the average overhead of the adaptive scheme in the RA scenario is significantly lower than that of the fixed scheme, corresponding to an overhead reduction of about 38%. In the CEA scenario, the average overhead of the adaptive scheme is reduced by about 30% compared with the fixed scheme. Meanwhile, in the CA scenario, the average overhead of the adaptive scheme is slightly higher than

that of the fixed scheme, by about 2% to 3%. These results confirm that adaptive pilot insertion is beneficial only when the pilot adjustment mechanism can effectively reduce the pilot density without causing a significant loss in estimation quality. In more challenging channel conditions, such as the CA scenario, the system is forced to increase the pilot density in order to maintain channel tracking capability, thereby losing the main advantage of the adaptive scheme.

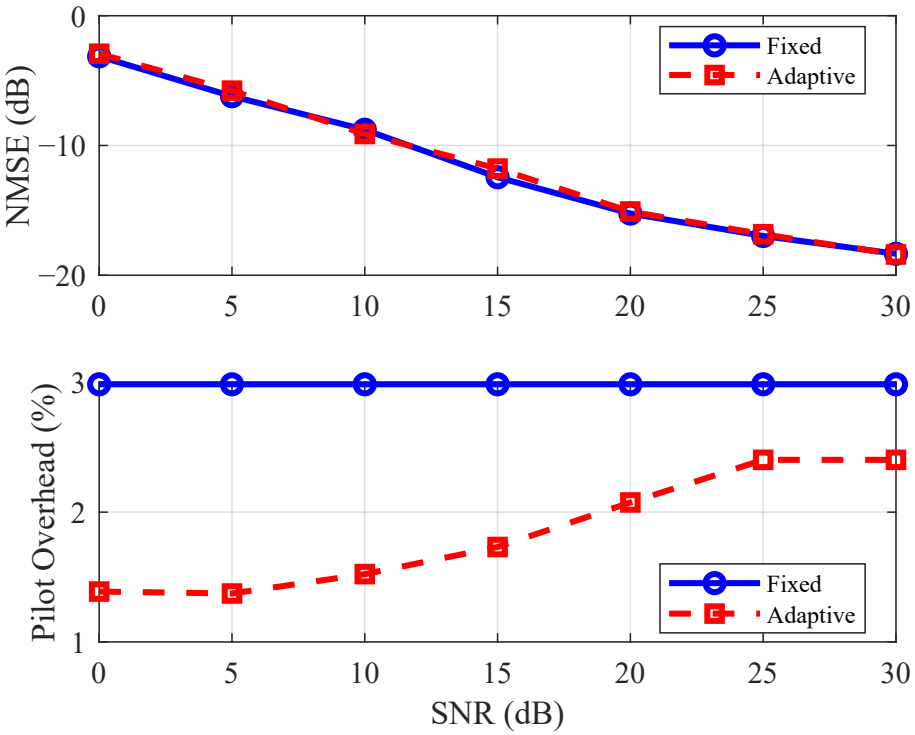


Figure 3. Adaptive pilot results for RA scenario.

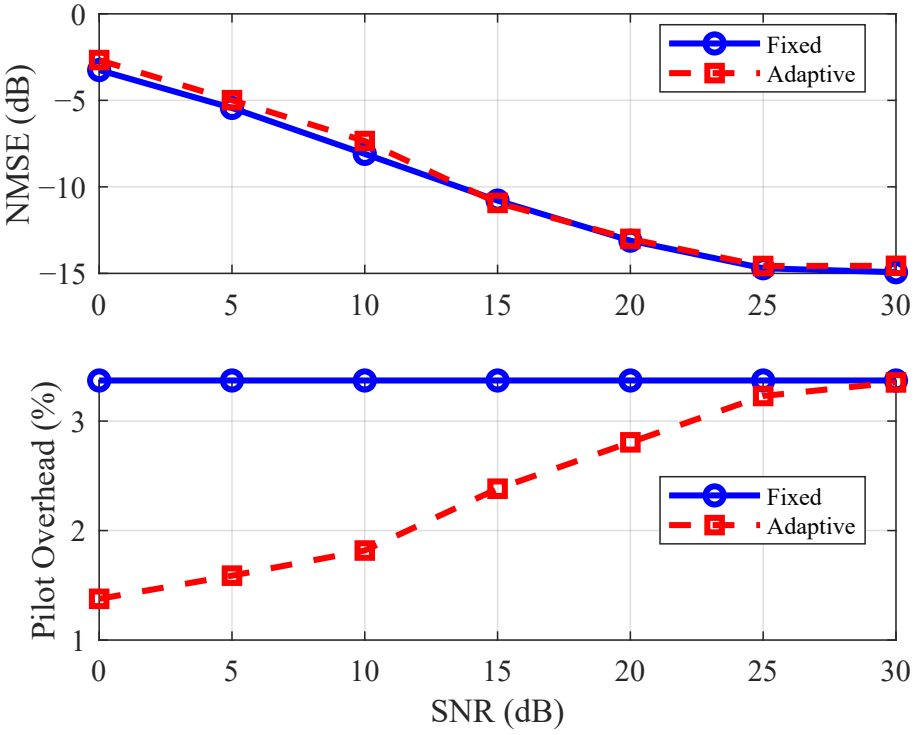


Figure 4. Adaptive pilot results for CEA scenario.

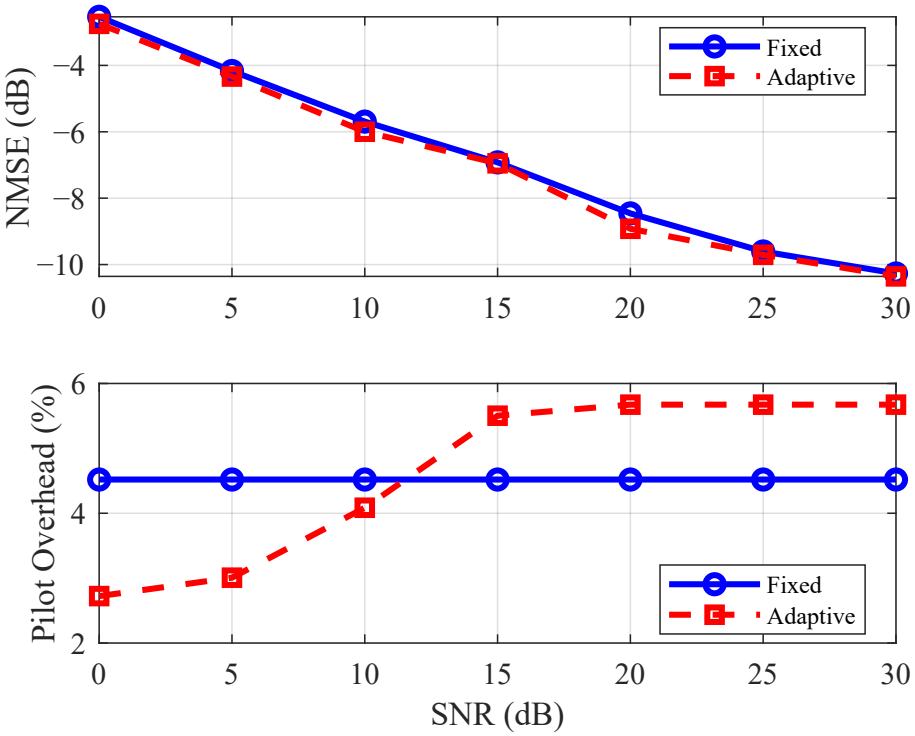


Figure 5. Adaptive pilot results for CA scenario.

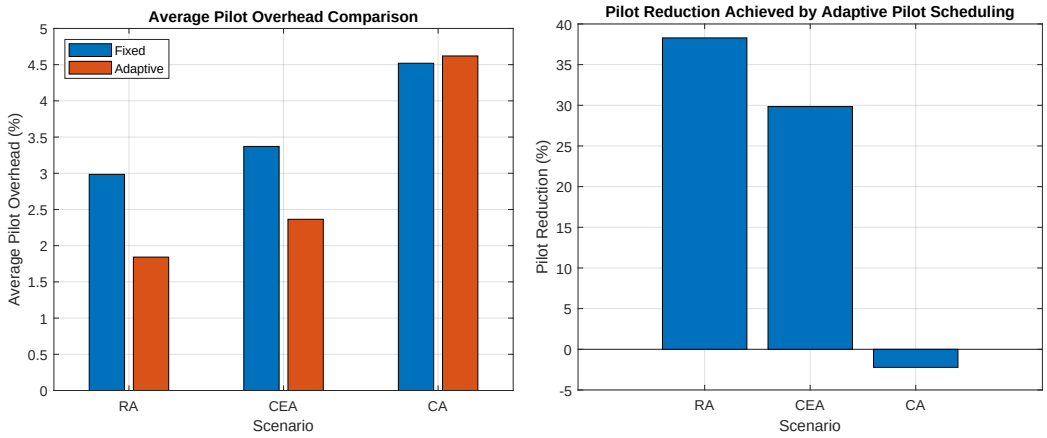


Figure 6. Adaptive pilot overhead comparisons.

Therefore, the proposed CA-API mechanism should not be viewed as an overhead-minimization scheme under all propagation conditions. In relatively stable environments such as RA and, to a lesser extent, CEA, it reduces pilot overhead while preserving estimation quality. Under the more dispersive CA condition, however, the adaptive controller shifts to a reliability-oriented mode and intentionally selects denser pilot insertion to maintain robust channel tracking.

4.2. Results and Discussion of Channel Estimation Algorithms

Figures 7–9 illustrate the NMSE and SER performance of the considered channel estimation algorithms under the RA, CEA, and CA conditions, respectively. Along with the three time-domain estimators, DFT-LMMSE is included as a conventional baseline. Overall, consistent trends are observed across both reconstruction and communication metrics: GPR provides the best performance, AR yields intermediate results, and PCHIP remains competitive as a low-complexity solution, while DFT-LMMSE serves as a reliable conventional reference. These results indicate that exploiting temporal channel correlation

is essential for accurate channel reconstruction in rapidly time-varying HSR environments. Since PCHIP primarily relies on local shape-preserving interpolation between pilot observations, its ability to capture fast channel fluctuations is limited. By contrast, AR enhances the estimation accuracy by tracking the symbol-to-symbol channel evolution, whereas GPR offers the most effective reconstruction due to its probabilistic regression capability and superior modeling flexibility.

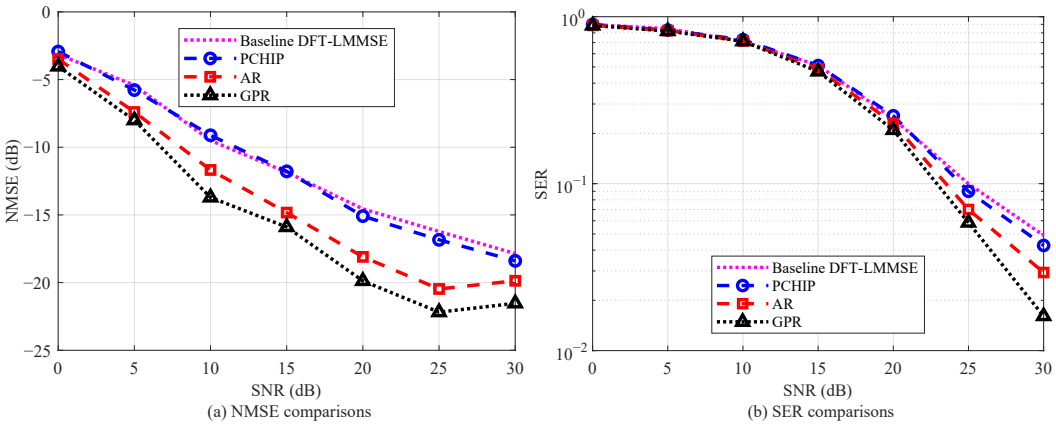


Figure 7. RA Scenario.

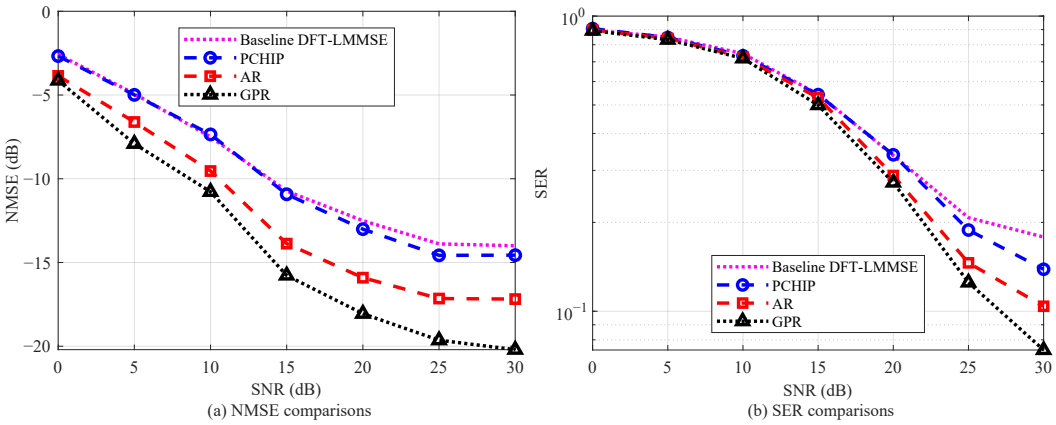


Figure 8. CEA Scenario.

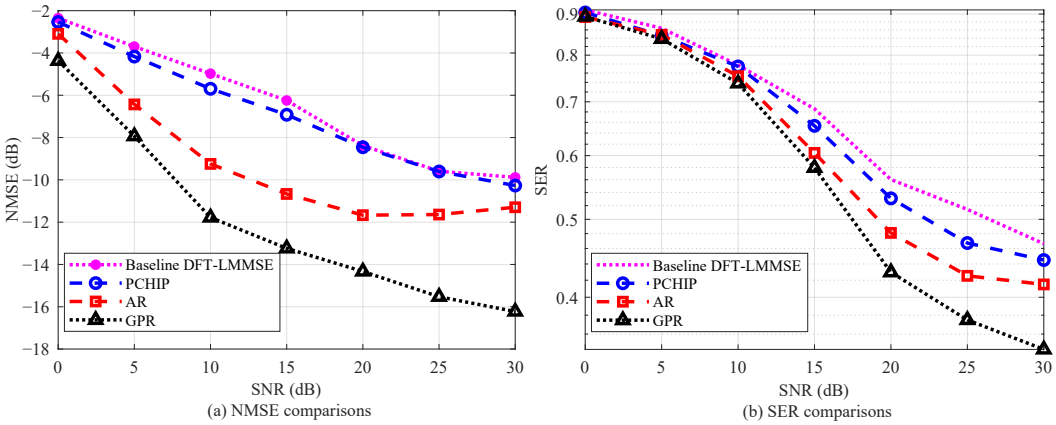


Figure 9. CA Scenario.

In the RA scenario shown in Figure 7, the evaluated algorithms exhibit a relatively stable separation across the SNR range. At low SNR, their NMSE values are closely aligned since the estimation accuracy is primarily noise-limited. However, as the SNR increases, the performance gap becomes more evident. At high SNR, GPR achieves an NMSE of

approximately −22 dB, outperforming AR and PCHIP, which reach roughly −20 dB and −18 dB, respectively, whereas the DFT-LMMSE baseline delivers a comparable yet slightly lower precision. This result indicates that, even in a mildly varying channel, the statistical learning capability of GPR still offers a meaningful gain over both deterministic interpolation and linear prediction. AR also maintains a clear advantage over PCHIP and the DFT-LMMSE baseline, demonstrating that temporal modeling is already beneficial even when channel variation is not severe. The SER results confirm the same ranking, with GPR consistently achieving the lowest error rates across the entire SNR range. Furthermore, AR continues to surpass both PCHIP and DFT-LMMSE, while PCHIP performs similarly to the conventional baseline despite its significantly reduced structural complexity.

The superiority of GPR becomes more pronounced in the CEA scenario in Figure 8. As the channel variation becomes more complicated, PCHIP begins to lose effectiveness more rapidly. This is particularly evident in the medium-SNR region (10 to 20 dB), where its NMSE curve exhibits a slower rate of improvement compared with those of AR, GPR, and the DFT-LMMSE baseline. By contrast, AR continues to track the channel evolution effectively, maintaining a moderate but consistent gain over PCHIP. GPR remains the best-performing method over the entire SNR range and achieves an NMSE of about −20 dB at 30 dB SNR, compared with roughly −17 dB for AR, about −14.5 dB for PCHIP, while the DFT-LMMSE baseline performs at a comparable yet slightly lower accuracy. The same ordering is also observed in SER results, where GPR achieves the lowest SER, AR outperforms both PCHIP and DFT-LMMSE, and PCHIP remains competitive despite its lower structural complexity. This behavior suggests that the CEA scenario already requires a more flexible estimator capable of describing non-stationary channel fluctuations beyond what deterministic interpolation can offer.

The CA scenario in Figure 9 represents the most challenging case among the three evaluated environments. Under these conditions, the NMSE performance of all methods degrades compared with the RA and CEA scenarios, reflecting the impact of more rapid fast fading and severe channel dynamics. Nevertheless, GPR still demonstrates remarkable robustness and maintains superior performance across the entire SNR range. At an SNR of 30 dB, GPR maintains an NMSE below approximately −16 dB, whereas AR and PCHIP only achieve around −11 dB and −10 dB, respectively. Meanwhile, the DFT-LMMSE baseline exhibits comparable yet slightly inferior performance. Another notable observation is the performance saturation encountered by both PCHIP and AR at high SNRs, indicating that their reconstruction capability becomes the dominant limiting factor once the noise level is sufficiently reduced. In contrast, GPR preserves a significant estimation gain, implying that its kernel-based statistical structure is better suited to capturing the strong Doppler-induced temporal correlations inherent in this severe scenario. This ranking is further supported by the SER results, where GPR consistently achieves the lowest SER. Furthermore, AR outperforms both PCHIP and DFT-LMMSE, while PCHIP remains competitive despite its lower computational complexity. These findings further confirm that in the CA scenario, estimators that explicitly exploit temporal channel evolution offer a clear advantage over standalone transform-domain denoising, with GPR's superiority evidenced in both NMSE and end-to-end communication performance.

Overall, the results in all three scenarios lead to two main conclusions. First, the relative gain of advanced estimators becomes increasingly visible as the SNR grows, because the impact of noise gradually diminishes and the intrinsic reconstruction capability of the algorithm becomes dominant. Second, the advantage of GPR becomes larger as the channel environment becomes more challenging, demonstrating its stronger adaptability to complex HSR propagation conditions in both NMSE and SER. Therefore, among the considered methods, GPR is the most effective channel estimator, the symbol-domain AR estimator

provides a robust intermediate solution with better accuracy than interpolation and a clear advantage over the DFT-LMMSE baseline, and PCHIP mainly serves as a low-complexity benchmark, offering the simplest structure despite its weaker NMSE performance.

4.3. Computational Complexity Analysis

Table 2 summarizes the computational complexity of the considered channel estimation methods, including DFT-LMMSE as a conventional baseline along with the three TDCE methods. The complexity is expressed in terms of the number of pilot observations N_p, the number of channel taps N_P, the number of OFDM symbols N_{sym}, and the number of reconstructed time-domain samples N_t. It should be noted that Table 2 summarizes the dominant asymptotic order only. In particular, for GPR, the practical implementation cost is also affected by kernel evaluation, hyperparameter handling, repeated regression fitting, and memory usage, which are not fully captured by the simplified order expression alone.

Table 2. Computational complexity of the considered channel estimation methods.

Method	Number of Operations	Complexity
PCHIP	$N_P(N_p + N_t)$	$\mathcal{O}(N_P N_t)$
AR	$N_P(N_{\text{sym}} + N_t)$	$\mathcal{O}(N_P N_t)$
GPR	$N_P(N_p^3 + N_p N_t)$	$\mathcal{O}\Big(N_P(N_p^3 + N_p N_t)\Big)$
DFT-LMMSE	$N_P\big(N_{\text{FFT}} \log N_{\text{FFT}} + N_p\big)$	$\mathcal{O}\big(N_P N_{\text{FFT}} \log N_{\text{FFT}}\big)$

For the three considered TDCE methods, PCHIP and AR have comparable computational order, whereas GPR is significantly more complex. Specifically, PCHIP reconstructs each channel tap directly from the pilot-domain samples over the full time grid, resulting in a complexity of $\mathcal{O}\big(N_P(N_p + N_t)\big) \approx \mathcal{O}(N_P N_t)$. Similarly, AR first performs channel tracking on the OFDM symbol grid and then interpolates over the complete time grid, leading to $\mathcal{O}\big(N_P(N_{\text{sym}} + N_t)\big) \approx \mathcal{O}(N_P N_t)$. Meanwhile, GPR requires covariance matrix inversion for the N_p pilot observations and prediction over the N_t reconstructed samples, which yields a higher complexity of $\mathcal{O}\Big(N_P(N_p^3 + N_p N_t)\Big)$.

Although PCHIP and AR have the same asymptotic order, PCHIP remains the least computationally demanding method because it only performs direct interpolation over the reconstructed time grid. AR has a slightly higher practical cost due to the additional symbol-domain tracking stage before interpolation. Regarding the DFT-LMMSE baseline, a higher practical computational burden is observed compared with PCHIP, as it involves transform-domain processing and LMMSE-based filtering in conjunction with pilot-domain estimation. Its dominant complexity arises from FFT/IFFT operations and transform-domain weighting, denoted as $\mathcal{O}(N_p N_{FFT} \log N_{FFT})$ in this simplified implementation. Notably, GPR is significantly more complex because of the covariance matrix inversion term N_p^3, which becomes dominant when the number of pilot observations increases. Therefore, PCHIP is the most attractive choice for low-complexity implementation; AR provides a favorable balance between complexity and tracking capability, whereas GPR is better suited to accuracy-oriented settings where higher computational cost can be tolerated.

To complement the complexity analysis, the practical runtime of the evaluated estimators was assessed. For a fair comparison, all algorithms were evaluated under the adaptive pilot scheme in the RA scenario at SNR = 20 dB using identical simulation conditions. The average runtime per estimator call was 9.47×10^{-2} ms for PCHIP, 2.12×10^{-1} ms for the DFT-LMMSE baseline, 3.03×10^{-1} ms for AR, and 2.23×10^{1} ms for GPR. These results are consistent with the theoretical complexity analysis. PCHIP is the most computationally efficient method, with a runtime slightly lower than that of the DFT-LMMSE baseline while providing comparable performance. AR incurs a moderate computational overhead,

whereas GPR shows substantially higher latency due to the repeated regression fitting and prediction steps.

Although GPR achieves the best estimation accuracy, its direct implementation is computationally demanding due to covariance–matrix inversion and repeated regression fitting. Therefore, GPR is considered in this work mainly as an accuracy-oriented estimator rather than a lightweight real-time solution. Several lightweight GPR strategies, such as sparse approximations, inducing-point methods, nearest-neighbor GPR, and distributed/local approximations, have been reported to reduce the computational and memory burden of standard GPR [32]. Integrating such accelerated GPR variants into the proposed HSR framework will be considered in future work.

5. Conclusions

This paper investigated an adaptive pilot-assisted channel estimation framework for HSR-OFDM systems by combining the CA-API mechanism, LMMSE shrinkage, and three time-domain estimators, including PCHIP, AR, and GPR, under measurement-based non-stationary channel conditions. The results show that the benefit of adaptive pilot scheduling is strongly scenario-dependent: the average pilot overhead is reduced by about 38% in RA and 30% in CEA, while in the more dispersive CA scenario, the controller increases pilot density to preserve reliable tracking. In both NMSE and SER evaluations, including comparison with the conventional DFT-LMMSE baseline, GPR achieves the best overall performance, AR provides a balanced trade-off between accuracy and complexity, and PCHIP remains attractive as the lowest-complexity method despite its lower estimation accuracy. The measured runtime at SNR = 20 dB is also consistent with the complexity analysis, confirming that adaptive pilot scheduling, estimation accuracy, communication performance, and implementation cost should be jointly considered in complexity-aware HSR wireless system design. Future work may investigate lightweight GPR variants and reinforcement-learning-based pilot-control strategies, such as proximal policy optimization (PPO) [33], for more complex joint optimization settings.

Author Contributions: Conceptualization, D.V.H. and T.T.D.; methodology, D.V.H. and K.V.N.; software, K.V.N. and D.V.H.; validation, D.V.H. and K.V.N.; formal analysis, D.V.H. and T.T.D.; investigation, K.V.N., D.V.H. and T.T.D.; resources, T.T.D.; writing—original draft preparation, K.V.N.; writing—review and editing, D.V.H. and T.T.D. All authors have read and agreed to the published version of the manuscript.

Funding: This research is funded by the University of Transport and Communications (UTC) under grant number T2024-DT-001TD.

Data Availability Statement: Data are contained within the article.

Conflicts of Interest: The authors declare no conflicts of interest.

References

1. Zhang, Q.; Dong, H.; Zhao, J. Channel Estimation for High-Speed Railway Wireless Communications: A Generative Adversarial Network Approach. *Electronics* **2023**, *12*, 1752. [CrossRef]
2. Siriwanitpong, A.; Sanada, K.; Hatano, H.; Mori, K.; Boonsrimuang, P. Deep Learning-Based Channel Estimation with 1D CNN for OFDM Systems Under High-Speed Railway Environments. *IEEE Access* **2025**, *13*, 13128–13142. [CrossRef]
3. Nguyen, V.D.; Ha, D.V.; Duong, V.V.; Le, H.A.; Nguyen, T.H. Joint fast time domain channel estimation with ICI cancellation for LTE-R systems. *Phys. Commun.* **2021**, *47*, 101349. [CrossRef]
4. Chen, X.; Chen, W.; Gong, X.; Ai, B.; Wassell, I. Wireless channel estimation for high-speed rail communications: Challenges, solutions and future directions. *High-Speed Railw.* **2023**, *1*, 18–22. [CrossRef]
5. Yao, L.; Md Johar, M.G.; Tham, J. Design and Research of Channel Estimation in OFDM Systems Based on High-Speed Channels. In *Proceedings of the AICI 2025: 2025 International Conference on Artificial Intelligence and Computational Intelligence*; ACM: New York, NY, USA, 2025; pp. 500–506. [CrossRef]

6. Yang, L.; Ren, L.; Shao, Y.; Chang, A. Meta-Learning based Time-varying Channel Estimation with ICI Cancellation in High-speed Mobile OFDM Systems. *Res. Sq.* **2023**. [CrossRef]
7. Junior, W.d.S.; Abrão, T. Machine learning-based methods for joint detection-channel estimation in OFDM systems. *Internet Technol. Lett.* **2023**, *6*, e404. [CrossRef]
8. Xu, M.; Zhang, S.; Ma, J.; Dobre, O.A. Deep Learning-Based Time-Varying Channel Estimation for RIS Assisted Communication. *IEEE Commun. Lett.* **2022**, *26*, 94–98. [CrossRef]
9. Shahmohammadi, M.; Sebghati, M.; Zareian, H. Deep Learning-based Pilot Adaptation and Channel Estimation in OFDM Systems. *Wirel. Pers. Commun.* **2024**, *134*, 915–933. [CrossRef]
10. Hu, R.H. Machine Learning-Enabled Channel Estimation for Massive MIMO in High-Speed Railway Communications. *Phys. Commun.* **2026**, *76*, 103091. [CrossRef]
11. Tang, Q.; Long, H.; Yang, H.; Li, Y. An enhanced LMMSE channel estimation under high speed railway scenarios. In *Proceedings of the 2017 IEEE International Conference on Communications Workshops (ICC Workshops)*; IEEE: Piscataway, NJ, USA, 2017; pp. 999–1004. [CrossRef]
12. Ma, Y.; Ai, B.; Ma, G.; Shafie, A.; Cheng, Q.; Yang, M.; Li, J.; Pang, X.; Yuan, J.; Zhong, Z. Channel Spreading Function-Inspired Channel Transfer Function Estimation for OFDM Systems with High Mobility. *IEEE Wirel. Commun. Lett.* **2025**, *14*, 2169–2173. [CrossRef]
13. Zhao, Y.; Zhao, W.; Wang, G.; Ai, B.; Putra, H.H.; Juliyanto, B. AoA-based channel estimation for massive MIMO OFDM communication systems on high speed rails. *China Commun.* **2020**, *17*, 90–100. [CrossRef]
14. Zhao, M.; Liu, Y.; Huang, J.; He, R.; Zhang, J.; Yu, C.; Wang, C. Artificial intelligence based multi-scenario mmWave channel modeling for intelligent high-speed train communications. *China Commun.* **2024**, *21*, 260–272. [CrossRef]
15. Khan, I.; Cheffena, M. Optimal pilot pattern for data-aided channel estimation for MIMO-OFDM wireless systems. *IET Commun.* **2024**, *18*, 1474–1484. [CrossRef]
16. Wan, Y.; Liu, A.; Quek, T.Q.S. Multi-User Pilot Pattern Optimization for Channel Extrapolation in 5G NR Systems. *IEEE Trans. Wirel. Commun.* **2025**, *24*, 6166–6179. [CrossRef]
17. Rao, R.M.; Marojevic, V.; Reed, J.H. Adaptive Pilot Patterns for CA-OFDM Systems in Nonstationary Wireless Channels. *IEEE Trans. Veh. Technol.* **2018**, *67*, 1231–1244. [CrossRef]
18. Abboud, M.K.; Sabbar, B.M. Performance evaluation of high mobility OFDM channel estimation techniques. *Int. J. Electr. Comput. Eng. (IJECE)* **2020**, *10*, 2562–2568. [CrossRef]
19. Yao, L.; Johar, M.G.M.; Tham, J. Design and Research of High Speed Channel Estimation Algorithm in OFDM System Based on GCE-RNN Algorithm. *J. Appl. Res. Ind. Eng.* **2025**, *12*, 525–540. [CrossRef]
20. Ahmad, M.; Shakeel, T.; Shin, S.Y. Image super resolution based channel estimation for future wireless communication. *Comput. Netw.* **2023**, *237*, 110057. [CrossRef]
21. Ha, T.; Jung, C.; Kim, H.; Park, J.; Park, J. Attention-Aided MMSE for OFDM Channel Estimation: Learning Linear Filters with Attention. *arXiv* **2025**, arXiv:2506.00452. [CrossRef]
22. Lv, C.; Luo, Z. Deep Learning for Channel Estimation in Physical Layer Wireless Communications: Fundamental, Methods, and Challenges. *Electronics* **2023**, *12*, 4965. [CrossRef]
23. Li, B.; Zheng, Q.; Tian, X.; Yang, M.; Gui, G.; Jiang, W.; Lei, H.; Jiang, J.; Shu, F.; Elhanashi, A.; et al. A Survey of Artificial Intelligence Enabled Channel Estimation Methods: Recent Advance, Performance, and Outlook. *Artif. Intell. Rev.* **2025**, *58*, 187. [CrossRef]
24. Essai Ali, M.H. Deep learning-based pilot-assisted channel state estimator for OFDM systems. *IET Commun.* **2020**, *15*, 257–264. [CrossRef]
25. Soltani, M.; Pourahmadi, V.; Sheikhzadeh, H. Pilot Pattern Design for Deep Learning-Based Channel Estimation in OFDM Systems. *IEEE Wirel. Commun. Lett.* **2020**, *9*, 2173–2176. [CrossRef]
26. Simeon, R.; Kim, T.; Perrins, E. Machine Learning with Gaussian Process Regression For Time-Varying Channel Estimation. In Proceedings of the ICC 2022—IEEE International Conference on Communications, Seoul, Republic of Korea, 16–20 May 2022; pp. 3400–3405. [CrossRef]
27. Bi, Y.; Zhang, J.; Zhu, Q.; Zhang, W.; Tian, L.; Zhang, P. A Novel Non-Stationary High-Speed Train (HST) Channel Modeling and Simulation Method. *IEEE Trans. Veh. Technol.* **2019**, *68*, 82–92. [CrossRef]
28. Ghazal, A.; Wang, C.X.; Ai, B.; Yuan, D.; Haas, H. A Nonstationary Wideband MIMO Channel Model for High-Mobility Intelligent Transportation Systems. *IEEE Trans. Intell. Transp. Syst.* **2014**, *16*, 885–897. [CrossRef]
29. Liu, L.; Tao, C.; Qiu, J.; Chen, H.; Yu, L.; Dong, W.; Yuan, Y. Position-Based Modeling for Wireless Channel on High-Speed Railway under a Viaduct at 2.35 GHz. *IEEE J. Sel. Areas Commun.* **2012**, *30*, 834–845. [CrossRef]
30. Zhanlav, T.; Mijiddorj, R. Convexity and monotonicity properties of the local integro cubic spline. *Appl. Math. Comput.* **2017**, *293*, 131–137. [CrossRef]

31. Buyuksar, A.B.; Senol, H.; Erkucuk, S.; Cirpan, H.A. Data-aided autoregressive sparse channel tracking for OFDM systems. In *Proceedings of the 2016 International Symposium on Wireless Communication Systems (ISWCS)*; IEEE: Piscataway, NJ, USA, 2016; pp. 424–428. [CrossRef]
32. Yuan, Z.; Zhu, M. Lightweight Distributed Gaussian Process Regression for Online Machine Learning. *IEEE Trans. Autom. Control* **2024**, *69*, 3928–3943. [CrossRef]
33. Ma, Z.; Zhang, R.; Ai, B.; Lian, Z.; Zeng, L.; Niyato, D.; Peng, Y. Deep Reinforcement Learning for Energy Efficiency Maximization in RSMA-IRS-Assisted ISAC System. *IEEE Trans. Veh. Technol.* **2025**, *74*, 18273–18278. [CrossRef]

Disclaimer/Publisher's Note: The statements, opinions and data contained in all publications are solely those of the individual author(s) and contributor(s) and not of MDPI and/or the editor(s). MDPI and/or the editor(s) disclaim responsibility for any injury to people or property resulting from any ideas, methods, instructions or products referred to in the content.